Single-Frequency Imaging and Material Characterization Using Reconfigurable Reflectarrays

Weite Zhang, Hipolito Gomez-Sousa, *Senior Member, IEEE*, Juan Heredia-Juesas, and Jose A. Martinez-Lorenzo, *Senior Member, IEEE*

***Abstract*— Conventional security screening systems cannot operate in real time and often suffer from false alarms due to the profile-only imaging without further analysis on the object material properties. Reflectarrays were recently proposed as devices capable of performing real-time security screening using a single-frequency radar signal. This article presents first a physical optics (PO)-based simulation method to facilitate the design of a multireflectarray system. Then, an object material characterization method using geometrical optics (GO) is derived for such a system. The characterization process not only retrieves the complex relative permittivity of the object but also improves its profile reconstruction in terms of a more accurate thickness. Both simulations and experiments are carried out to verify the effectiveness and efficiency of the proposed methods. Primary results show great potentials for security screening, especially in scenarios where the inspection of human bodies for threat materials, such as narcotics and explosives, is required.**

***Index Terms*— Geometrical optics (GO), material characterization, physical optics (PO), profile reconstruction, reflectarray, security screening, single frequency.**

I. Introduction

MICROWAVE and millimeter-wave (mm-wave) have been successfully used in various security screening applications [1]–[3]. This is due to the fact that: 1) they are nonionizing radiation, making them safe to be used in public spaces, and 2) they can penetrate many optically opaque materials, enabling 3-D reconstruction of objects concealed under clothing. Conventional security screening systems–such as those working in monostatic, bistatic, and multistatic configuraions [4]–[6]–often require large frequency bandwidth and stringent interchannel coherence. These requirements not only make imaging frequency-dispersive objects more challenging but also increase the system design complexity and cost. Advanced screening systems using compressive sensing (CS) [7]–[9] have been proposed to achieve lower system complexity and higher imaging resolution with respect to those of conventional ones [10]. However, CS algorithms still need intensive digital signal processing (DSP), which sets a heavy computational cost at the receiving end and therefore limits their use in real-time applications.

Recently, a reflectarray system has been demonstrated to perform real-time security screening [11]–[13]. The reflectarray is made of thousands of 1-bit, phase-adaptable patch antennas [14], [15], which enable multiscale, beam focusing and imaging of targets located within a region of interest (RoI). Such a system annihilates the software-based computational cost of DSP imaging algorithms by the replacement with hardware-based focused imaging. In addition, not only it produces high-resolution images but also operates in real time; this is because the reflectarray is illuminated with a few transceiver antennas excited with a single-frequency continuous-wave (CW) signal. Notwithstanding, the single-frequency scheme only permits its use in the near-field region, which, in this case, has a maximum range of ≈ 2 m.

To evaluate the performance of the electrically large reflectarray, state-of-the-art full-wave simulations, such as those based on the multilevel fast multipole algorithm (MLFMA) [16] and the method of moments (MoM) [17], require a lot of computational resources and a large amount of time. Thus, optimizing and designing such reflectarray-based screening systems are challenging. In [13], an optimized physical optics (PO) method using multiple CPU threads was proposed to simulate a single-reflectarray-based imaging system in a reasonable amount of time. However, common high-throughput screening scenarios require to image many targets distributed over a wide region [18]–[20], where multiple reflectarrays are needed to cover the entire imaging domain. Consequently, a more general PO-based method to simulate the performance of a multireflectarray system is a necessity.

Moreover, even in well-designed reflectarray systems with good imaging resolution, frequent false alarms still happen due to the object profile-only imaging with no information on its material properties. This ultimately results in uncomfortable

Manuscript received November 25, 2020; revised January 15, 2021; accepted February 6, 2021. Date of publication March 10, 2021; date of current version July 1, 2021. This work was supported in part by the NSF CAREER Program under Award 1653671 and in part by the U.S. Department of Homeland Security under Award 2013-ST-061-ED0001. *(Corresponding author: Jose A. Martinez-Lorenzo.)*

Weite Zhang is with the Department of Electrical and Computer Engineering, Northeastern University, Boston, MA 02115 USA (e-mail: zhang.weit@northeastern.edu).

Hipolito Gomez-Sousa, Juan Heredia-Juesas, and Jose A. Martinez-Lorenzo are with the Department of Electrical and Computer Engineering, Northeastern University, Boston, MA 02115 USA, and also with the Department of Mechanical and Industrial Engineering, Northeastern University, Boston, MA 02115 USA (e-mail: j.martinez-lorenzo@northeastern.edu).

Color versions of one or more figures in this article are available at https://doi.org/10.1109/TMTT.2021.3061597.

Digital Object Identifier 10.1109/TMTT.2021.3061597

pat-downs and reduced systems' throughput. One straightforward solution to discriminate objects between hazardous and innocuous materials is by characterizing their object-complex permittivities. The characterization can be done using the transmitted and received electromagnetic fields in different ways [21]. However, several drawbacks remain to be addressed before they can be efficiently used in realistic security screening applications. These include but are not limited to the following: 1) the need to use multiple transceivers or a large frequency bandwidth [22]–[24], which may result in challenging detection and classification of frequency-dispersive objects [25]–[27], and 2) the need to incorporate either the object thickness, boundaries, or location as *prior* information in the estimation process [28]–[31]. Therefore, more advanced material characterization in addition to the object profile imaging is of great importance for the reflectarray system.

In this article, we first present an efficient and effective PO method to simulate the imaging performance of a people screening system using multiple reflectarrays. Then, a single-frequency material characterization method using a geometrical optics (GO) forward model is proposed, where no aforementioned *prior* information is required in the estimation process. In addition, unlike conventional material characterization methods using multiple frequencies to solve the 2π phase ambiguity, this method is based on the range-dependent focused radiation to form multiple spatially independent measurements. Note that such a phase ambiguity [32], [33], if not solved, will lead to a failure in discriminating any two dielectric objects satisfying $T_1\sqrt{\varepsilon_1'} = T_2\sqrt{\varepsilon_2'}$, where T_i and ε_i', $i \in \{1, 2\}$, are the thickness and dielectric constant, respectively.

The rest of this article is organized as follows. In Section II, the concept of personal screening systems using multiple active reflectarrays is briefly described. In Section III, the theory on the PO and GO methods is proposed. In Section IV, two-reflectarray-based simulations and experiments are carried out to detect dielectric objects at a single microwave frequency of 24.16 GHz. Section V summarizes this article.

II. System Concept

The original idea of using multiple active reflectarrays in people-screening system was pioneered by Smiths Detection Inc. [11], [12]. As shown in Fig. 1, the system has two principal components: 1) the feeding antennas that are used to transmit and receive the single-frequency CW radar signal and 2) the reflectarrays that are used to focus on the CW signal at a point in the RoI, when used in transmission mode, and to refocus the scattered field from that point into the receiving antennas, when used in receiving mode. In this setup, a potentially concealed dielectric object in the RoI has an unknown profile and complex relative permittivity $\varepsilon_r = \varepsilon_r' - j\varepsilon_r''$, where ε_r' and ε_r'' are the dielectric constant and loss factor, respectively.

Note that each reflectarray is equipped with a single horn antenna and transceiver module, and several reflectarrays can be confocally configured to simultaneously focus at the same point in space and to perform the imaging. In the general

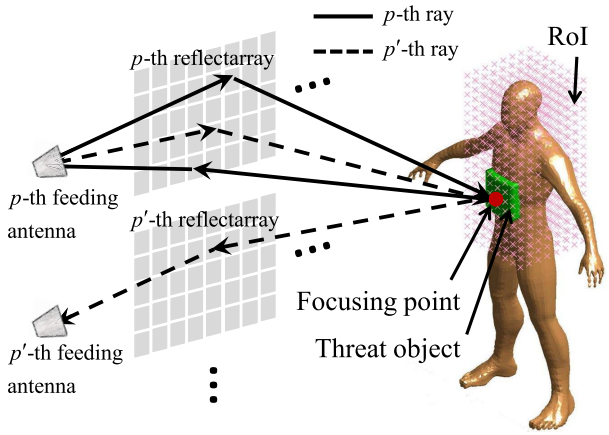

Fig. 1. System concept of microwave screening using multiple reflectarrays at 24.16 GHz, where the pth feeding antenna is active as a general analysis. The reflectarrays are all confocally configured to focus/refocus on the single-frequency CW signal at a specific point that can be scanned in the RoI. Each reflectarray has a corresponding feeding antenna for transmitting/receiving the radar signal. The concealed dielectric object under detection has an undetermined profile and complex relative permittivity.

configuration shown in Fig. 1, all P pairs of feeding antenna and reflectarrays (FARAs) are used as follows. First, the CW signal from the pth feeding antenna is used to illuminate its corresponding reflectarray. Then, this incident field is reflected from the reflectarray and focused at a point in the RoI; this is done by applying a binary phase to each reflectarray patch to make the free-space propagation phase of each horn/patch/focusing-point ray to be as close as possible to zero [34]–[36]. Next, the focused incident field interacts with the object, thus producing a new field that is scattered toward the imaging system. Due to the confocal configuration, the scattered field is refocused through the p'th receiving reflectarray toward its corresponding receiving antenna. Repeating the above procedure for all pairs of transmitting and receiving FARAs, an image of the target under test is finally created. Note that the use of multiple FARAs can provide an improved receiving signal-to-noise ratio (SNR) of P times that of the single FARA system from [13]. Here, P is the total number of FARAs employed.

In this article, the microwave operation frequency f_0 is selected to be 24.16 GHz. Although operating at higher frequencies can provide a better imaging resolution and a smaller hardware size, there are several considerations for using the 24-GHz band. First, the 24-GHz band is within the industrial, scientific, and medical (ISM) band, which provides the certification for its usage worldwide [37]. Second, hardware working at the 24-GHz band is relatively inexpensive due to the popular use at K-band for satellite communications. Third, the 24-GHz band meets the requirement of a good imaging resolution with an acceptable radar aperture size. Finally, at this frequency band, the clothing is essentially transparent [38], and the human skin is very reflective [39], which is measured to have a complex relative permittivity of $20 - j18.7$, corresponding to a relatively large reflectivity of 0.7. Although it is 0.3 less than that of the perfect electric conductor (PEC), it can provide a generally accepted approximation to model the human body

as the PEC. Thus, the proposed algorithms in this article reasonably assume that the human body is a flat PEC plate, considering some planar parts of the human body, such as the chest and belly.

III. Theoretical Analysis

A. PO-Based Simulation

To perform the performance simulation on a multirefelctaray system, all surfaces of the feeding horn apertures, patches on the reflectarrays, and targets are discretized into triangular facets. According to the exact free-space near-field equation described in [40], the incident electric field $\mathbf{E}_{\text{inc}}(\mathbf{r})$ and the magnetic field $\mathbf{H}_{\text{inc}}(\mathbf{r})$ at an observation point $\mathbf{r}$ can be computed using the electric $\mathbf{J}(\mathbf{r}')$ and magnetic $\mathbf{M}(\mathbf{r}')$ current sources, namely

$$\begin{aligned}\mathbf{E}_{\text{inc}}(\mathbf{r}) &= \int_S \{-A_1 G_1 \mathbf{J}(\mathbf{r}') - A_1 G_2 [\mathbf{J}(\mathbf{r}') \cdot \mathbf{R}]\mathbf{R} \\ &\quad - B_1 G_3 \mathbf{M}(\mathbf{r}') \times \mathbf{R}\} e^{-jk_0 R} ds \\ \mathbf{H}_{\text{inc}}(\mathbf{r}) &= \int_S \{-A_2 G_1 \mathbf{M}(\mathbf{r}') - A_2 G_2 [\mathbf{M}(\mathbf{r}') \cdot \mathbf{R}]\mathbf{R} \\ &\quad + B_2 G_3 \mathbf{J}(\mathbf{r}') \times \mathbf{R}\} e^{-jk_0 R} ds \end{aligned} \tag{1}$$

where $A_1 = (j\eta_0/4\pi k_0)$, $A_2 = (j/4\pi k_0 \eta_0^2)$; $B_1 = B_2 = (1/4\pi)$; $G_1 = (-1 - jk_0R + (k_0R)^2/R^3)$; $G_2 = (3 + j3k_0R - (k_0R)^2/R^5)$; $G_3 = (1 + jk_0R/R^3)$; $\mathbf{R} = \mathbf{r} - \mathbf{r}'$, $R = |\mathbf{R}|$ being the distance between the source point $\mathbf{r}'$ and the observation point $\mathbf{r}$; k_0 and η_0 are the wavenumber and impedance in free-space, respectively; $\mathbf{r}$ is the observation point; $\mathbf{r}'$ is the source point; j is the imaginary unit; and S is surface of the feeding antenna aperture.

With the incident fields $\mathbf{E}_{\text{inc}}$ and $\mathbf{H}_{\text{inc}}$, the induced electric $\mathbf{J}$ and magnetic $\mathbf{M}$ currents on any interface can be calculated using the modified equivalent current approximation (MECA) equations [41], [42], which represents a generalization of the PO for both conducting and nonconducting dielectric surfaces

$$\begin{aligned}\mathbf{J}(\mathbf{r}) &= \frac{1}{\eta_1}\big[E_{\text{inc}}^{\text{TE}} \cos\theta_{\text{inc}}(1 - R_{\text{TE}})\hat{\mathbf{e}}_{\text{TE}} \\ &\quad + E_{\text{inc}}^{\text{TM}}(1 - R_{\text{TM}})(\hat{\mathbf{n}}_0 \times \hat{\mathbf{e}}_{\text{TM}})\big]\big|_{S_{\text{B}}} \\ \mathbf{M}(\mathbf{r}) &= E_{\text{inc}}^{TE}(1 + R_{\text{TE}})(\hat{\mathbf{e}}_{\text{TM}} \times \hat{\mathbf{n}}_0) \\ &\quad + E_{\text{inc}}^{\text{TM}} \cos\theta_{\text{inc}}(1 + R_{\text{TM}})\hat{\mathbf{e}}_{\text{TE}}\big|_{S_{\text{B}}} \end{aligned} \tag{2}$$

where the incident electric field is decomposed into its transverse electric (TE) and transverse magnetic (TM) modes, S_B is the interface between the two media, η_1 is the wave impendence of the outwards medium, $\hat{\mathbf{n}}_0$ is the outward unit vector perpendicular to the interface, θ_{inc} is the incident angle, $E_{\text{inc}}^{\text{TE/TM}}$ and $\hat{\mathbf{e}}_{\text{TE/TM}}$ are the incident field magnitude and the corresponding unit vector of the TE/TM mode, respectively, and $R_{\text{TE/TM}}$ is the reflection coefficient of the TE/TM mode on the interface.

The definition of $R_{\text{TE/TM}}$ is as follows:

$$R_{\text{TE}}|_{\mu_1=\mu_2} = \frac{\cos\theta_{\text{inc}} - \sqrt{\frac{\varepsilon_2}{\varepsilon_1}}\sqrt{1 - \frac{\varepsilon_1}{\varepsilon_2}\sin^2\theta_{\text{inc}}}}{\cos\theta_{\text{inc}} + \sqrt{\frac{\varepsilon_2}{\varepsilon_1}}\sqrt{1 - \frac{\varepsilon_1}{\varepsilon_2}\sin^2\theta_{\text{inc}}}}$$

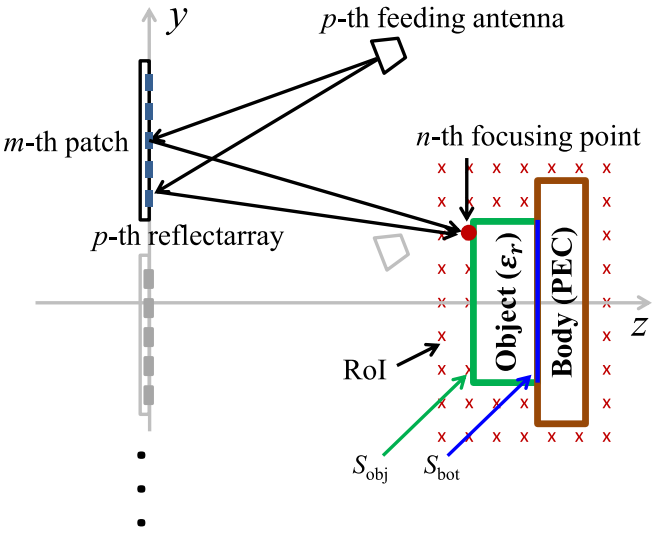

Fig. 2. Simulation model for the reconstruction of the threat profile. The body is assumed to be a flat PEC plate, and the threat attached on the body surface is a dielectric slab with undetermined profile and material in terms of the complex relative permittivity ε_r. S_{obj} and S_{bot} represent the air–object and object–body interface, respectively.

$$R_{\text{TM}}|_{\mu_1=\mu_2} = \frac{-\cos\theta_{\text{inc}} + \sqrt{\frac{\varepsilon_1}{\varepsilon_2}}\sqrt{1 - \frac{\varepsilon_1}{\varepsilon_2}\sin^2\theta_{\text{inc}}}}{\cos\theta_{\text{inc}} + \sqrt{\frac{\varepsilon_1}{\varepsilon_2}}\sqrt{1 - \frac{\varepsilon_1}{\varepsilon_2}\sin^2\theta_{\text{inc}}}} \tag{3}$$

where ε_1 and ε_2 are the complex permittivity of the outwards and inner medium, respectively, and μ_1 and μ_2 are the corresponding permeabilities assumed to be equal. Note that on the surface of the PEC, magnetic current $\mathbf{M} = 0$ due to the fact that $R_{\text{TE}} = R_{\text{TM}} = -1$. Therefore, the magnetic currents on the feeding antenna apertures, the patch elements on the reflectarrays, and the human body can be neglected.

As shown in Fig. 2, assuming that the total number of the patches on each reflectarray is M and the electric current distribution of the pth feeding antenna is $\mathbf{J}_p^{\text{inc}}$ ($p \in \{1, 2, \ldots, P\}$), the incident electric $\mathbf{E}_{m,p}^{\text{patch}}$ and magnetic $\mathbf{H}_{m,p}^{\text{patch}}$ fields on the mth patch ($m \in \{1, 2, \ldots, M\}$) can be obtained using (1). The corresponding induced electric current $\mathbf{J}_{m,p}^{\text{patch}}$ can be calculated based on (2).

The reflectarrays are confocally set to focus on the incident wavefront to a desired point by introducing the binary phase compensation $\Delta\psi_{n,m,p}$ to each patch element

$$\Delta\psi_{n,m,p} = \begin{cases} \pi, & \dfrac{\pi}{2} < \text{mod}(k_0 \cdot L_{n,m,p}, 2\pi) < \dfrac{3\pi}{2} \\ 0, & \text{otherwise} \end{cases} \tag{4}$$

where mod(·) is the modulus operator and $L_{n,m,p} = (|\mathbf{r}_p^{\text{feed}} - \mathbf{r}_{m,p}^{\text{patch}}| + |\mathbf{r}_{m,p}^{\text{patch}} - \mathbf{r}_n^{\text{focus}}|)$. $\mathbf{r}_p^{\text{feed}}$, $\mathbf{r}_{m,p}^{\text{patch}}$, and $\mathbf{r}_n^{\text{focus}}$ are the positions of the pth feeding antenna, the mth patch of the pth reflectarray, and the nth focusing point, respectively.

Therefore, the electric current is modified as $\mathbf{J}_{m,p}^{\text{patch}} e^{j\Delta\psi_{n,m,p}}$. Using (1), again, we can calculate the incident electric $\mathbf{E}_{m,n,p}^{\text{target}}$ and magnetic $\mathbf{H}_{m,n,p}^{\text{target}}$ fields on the target surface. Thus, the total incident electric $\mathbf{E}_{n,p}^{\text{target}}$ and magnetic $\mathbf{H}_{n,p}^{\text{target}}$ fields for the pth

feeding antenna and the nth focusing point are

$$\mathbf{E}_{n,p}^{\text{target}} = \sum_{m=1}^{M} \mathbf{E}_{m,n,p}^{\text{target}}$$
$$\mathbf{H}_{n,p}^{\text{target}} = \sum_{m=1}^{M} \mathbf{H}_{m,n,p}^{\text{target}}. \tag{5}$$

According to (2), the corresponding induced electric $\mathbf{J}_{n,p}^{\text{target}}$ and magnetic $\mathbf{M}_{n,p}^{\text{target}}$ currents can be written as

$$\mathbf{J}_{n,p}^{\text{target}} = \mathbf{J}_{n,p}^{\text{obj}} + \mathbf{J}_{n,p}^{\text{body}}$$
$$\mathbf{M}_{n,p}^{\text{target}} = \mathbf{M}_{n,p}^{\text{obj}} + \mathbf{M}_{n,p}^{\text{body}} \tag{6}$$

where $\mathbf{J}_{n,p}^{\text{obj}}$ and $\mathbf{M}_{n,p}^{\text{obj}}$ are the electric and magnetic currents, respectively, on the surface of the dielectric object. Similarly, $\mathbf{J}_{n,p}^{\text{body}}$ and $\mathbf{M}_{n,p}^{\text{body}}$ are the currents on the surface of the human body.

Note that $\mathbf{M}_{n,p}^{\text{body}} = 0$ for the human body (approximated to be PEC), and one can calculate $\mathbf{J}_{n,p}^{\text{body}}$ using the first-order PO method, while $\mathbf{J}/\mathbf{M}_{n,p}^{\text{obj}}$ must be calculated by considering multiple reflections within the dielectric object using a Kth-order PO method based on (1) and (2). The process can be described as

$$\begin{aligned}\mathbf{J}/\mathbf{M}_{n,p,0}^{\text{obj}} &\rightarrow \mathbf{E}/\mathbf{H}_{n,p,1}^{\text{bot}} \rightarrow \mathbf{J}/\mathbf{M}_{n,p,1}^{\text{bot}} \rightarrow \mathbf{E}/\mathbf{H}_{n,p,1}^{\text{obj}} \\ &\rightarrow \mathbf{J}/\mathbf{M}_{n,p,1}^{\text{obj}} \rightarrow \mathbf{E}/\mathbf{H}_{n,p,2}^{\text{bot}} \rightarrow \mathbf{J}/\mathbf{M}_{n,p,2}^{\text{bot}} \rightarrow \mathbf{E}/\mathbf{H}_{n,p,2}^{\text{obj}} \\ &\rightarrow \mathbf{J}/\mathbf{M}_{n,p,2}^{\text{obj}} \rightarrow \mathbf{E}/\mathbf{H}_{n,p,3}^{\text{bot}} \rightarrow \mathbf{J}/\mathbf{M}_{n,p,3}^{\text{bot}} \rightarrow \mathbf{E}/\mathbf{H}_{n,p,3}^{\text{obj}} \\ &\quad\vdots \\ &\rightarrow \mathbf{J}/\mathbf{M}_{n,p,K-1}^{\text{obj}}\end{aligned} \tag{7}$$

where $\mathbf{J}/\mathbf{M}_{n,p,0}^{\text{obj}}$ is denoted as the electric or magnetic currents induced by the initial reflection on the air–object interface S_{obj} and $\mathbf{E}/\mathbf{H}_{n,p,k}^{\text{bot}}$ and $\mathbf{J}/\mathbf{M}_{n,p,k}^{\text{bot}}$ are the incident fields and the induced currents, respectively, on the object–body interface S_{bot} after k ($k \in \{1, 2, \ldots, K-1\}$) reflections within the dielectric object. Similarly, $\mathbf{E}/\mathbf{H}_{n,p,k}^{\text{obj}}$ and $\mathbf{J}/\mathbf{M}_{n,p,k}^{\text{obj}}$ correspond to the incident fields and the induced currents, respectively, on S_{obj}. Consequently, the total electric $\mathbf{J}_{n,p}^{\text{obj}}$ and magnetic $\mathbf{M}_{n,p}^{\text{obj}}$ currents on S_{obj} are computed as follows:

$$\mathbf{J}_{n,p}^{\text{obj}} = \mathbf{J}_{n,p,0}^{\text{obj}} - \sum_{k=1}^{K-1} \mathbf{J}_{n,p,k}^{\text{obj}}$$
$$\mathbf{M}_{n,p}^{\text{obj}} = \mathbf{M}_{n,p,0}^{\text{obj}} - \sum_{k=1}^{K-1} \mathbf{M}_{n,p,k}^{\text{obj}}. \tag{8}$$

As all the reflectarrays are confocally arranged, all the receiving antennas are able to receive the scattered signal. Define $\mathbf{E}_{n,p}^{\text{rec}}$ as the total received electric field from the pth receiving antenna when all the P feeding antennas are active to focus the beam at $\mathbf{r}_n^{\text{focus}}$. Intuitively, $\mathbf{E}_{n,p}^{\text{rec}}$ can be calculated via an inverse computational procedure using the PO method from the target to the receiving horns based on (1) and (2). However, to improve the computational efficiency, a general reciprocity theorem for multiple-input–multiple-output (MIMO) systems is derived as follows:

$$E_{n,p}^{\text{rec}} = \frac{\int_S \mathbf{E}_{n,p}^{\text{target}} \cdot \mathbf{J}_n^{\text{target}} - \mathbf{H}_{n,p}^{\text{target}} \cdot \mathbf{M}_n^{\text{target}} ds}{\int_S \hat{\mathbf{e}}_{n,p}^{\text{rec}} \cdot \mathbf{J}_p^{\text{inc}} ds} \tag{9}$$

where $E_{n,p}^{\text{rec}}$ is the amplitude of the received field $\mathbf{E}_{n,p}^{\text{rec}}$, considered to be uniform on the receiving apertures; $\mathbf{J}_n^{\text{target}} = \sum_{p=1}^{P} \mathbf{J}_{n,p}^{\text{target}}$ and $\mathbf{M}_n^{\text{target}} = \sum_{p=1}^{P} \mathbf{M}_{n,p}^{\text{target}}$ are the total induced electric and magnetic currents on the target surface, respectively; and $\hat{\mathbf{e}}_{n,p}^{\text{rec}}$ represents the uniform complex polarization vector of $\mathbf{E}_{n,p}^{\text{rec}}$.

Finally, the target profile can be reconstructed by adding the received electric field $E_{n,p}^{\text{rec}}$ from all P receivers

$$E_n^{\text{rec}} = \sum_{p=1}^{P} E_{n,p}^{\text{rec}} \tag{10}$$

and determining the location of the maximum received field E_n^{rec} along the z-axis, namely

$$z_n^{\text{imaging}}(x_n, y_n) = \max_{z_n} \left\{ \left| E_n^{\text{rec}}(x_n, y_n, z_n) \right| \right\} \tag{11}$$

where (x_n, y_n, z_n) is the coordinates of the nth focusing point.

B. GO-Based Material Characterization

To ensure real-time prediction and classification of potential threat objects in the reflectarray screening system, it is desired to develop a fully analytical forward model for characterizing the complex relative permittivity of the object. To achieve this, we proposed a ray tracing-based GO method to predict the received electric fields $\tilde{E}_n^{\text{rec}}$ [43]. By sweeping the relative permittivity $\varepsilon_r = \varepsilon_r' - j\varepsilon_r''$ and the object thickness T, the analytical $\tilde{E}_n^{\text{rec}}(\varepsilon_r', \varepsilon_r'', T)$ are computed. $\tilde{E}_n^{\text{rec}}$ is then compared to the measured E_n^{rec} (or simulated with the full-wave method, such as the MLFMA used in this article) to find the best matched magnitude and phase responses. Consequently, the object thickness $\tilde{T}$ and relative permittivity $\tilde{\varepsilon}_r = \tilde{\varepsilon}_r' - j\tilde{\varepsilon}_r''$ are estimated by minimizing the difference between the modeled and measured receiving fields.

Fig. 3 shows the proposed GO forward model of the multireflectarray system. Assume that the pth feeding antenna at $\mathbf{r}_p^{\text{feed}}$ is active, and the ray that originates from $\mathbf{r}_p^{\text{feed}}$ and terminates at the p'th feeding antenna at $\mathbf{r}_{p'}^{\text{feed}}$ has an initial an amplitude of E_0. The complex incident amplitude $\tilde{E}_{m,p}^{\text{patch}}$ on the mth patch of the pth reflectarray can be computed by considering both magnitude loss and phase delay

$$\tilde{E}_{m,p}^{\text{patch}} = \frac{E_0 e^{-jk_0 \left| \mathbf{r}_{m,p}^{\text{patch}} - \mathbf{r}_p^{\text{feed}} \right|}}{\left| \mathbf{r}_{m,p}^{\text{patch}} - \mathbf{r}_p^{\text{feed}} \right|} \tag{12}$$

where $\mathbf{r}_{m,p}^{\text{patch}}$ is the position of the mth patch of the pth reflectarray.

Reflected from the pth reflectarray, which is assumed to focus the CW wave at the nth focusing point $\mathbf{r}_n^{\text{focus}}$, the ray will reach the air–object interface S_{obj} at the point $\mathbf{r}_{\text{obj}}$

$$\mathbf{r}_{\text{obj}} = \frac{z_{\text{bg}} - T}{\cos\theta_{n,m}^{\text{inc}}} \frac{\mathbf{r}_n^{\text{focus}} - \mathbf{r}_{m,p}^{\text{patch}}}{\left| \mathbf{r}_n^{\text{focus}} - \mathbf{r}_{m,p}^{\text{patch}} \right|} + \mathbf{r}_{m,p}^{\text{patch}} \tag{13}$$

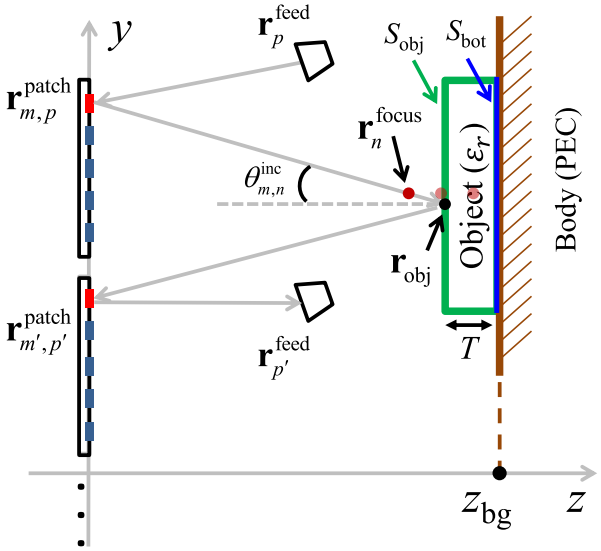

Fig. 3. GO model for the object material identification. All the rays, originating from the transmitting horns and terminating at the receiving horns, are considered for estimating the unknown complex relative permittivity ε_r and the thickness T. S_{obj} and S_{bot} represent the air-object and object–body interface, respectively. z_{bg} is the background range at S_{bot}.

where z_{bg} is the background range, namely the object–body interface S_{bot}, which can be known based on the PO-based profile reconstruction using (11); T is the unknown thickness of the dielectric object; and $\theta_{n,m}^{\text{inc}}$ is the incident angle. Note that the incident angle $\theta_{n,m}^{\text{inc}}$ will vary when focusing at different ranges, which essentially gives rise to multiple spatially independent measurements to solve the 2π phase ambiguity and the unknown object parameters [44].

Thus, the incident ray amplitude at $\mathbf{r}_{\text{obj}}$ can be calculated as

$$\tilde{E}_{n,m,p}^{\text{obj}} = -\frac{\tilde{E}_{m,p}^{\text{patch}}\, e^{-j\left[k_0\left(\left|\mathbf{r}_{\text{obj}}-\mathbf{r}_{m,p}^{\text{patch}}\right|\right)-\Delta\psi_{n,m,p}\right]}}{1+\left|\mathbf{r}_{\text{obj}}-\mathbf{r}_{m,p}^{\text{patch}}\right|/\left|\mathbf{r}_{m,p}^{\text{patch}}-\mathbf{r}_{p}^{\text{feed}}\right|} \tag{14}$$

where $\Delta\psi_{n,m,p}$ is the binary phase compensation added on the mth patch element of the pth reflectarray.

Scattered from the imaging domain, the backwards ray will illuminate upon the m'th patch of the p'th reflectarray at $\mathbf{r}_{m',p'}^{\text{patch}}$. Note that the subindexes m' and p' of $\mathbf{r}_{m',p'}^{\text{patch}}$ can be determined using ray tracing, which are merely dependent on $\mathbf{r}_{m,p}^{\text{patch}}$ and $\mathbf{r}_{\text{obj}}$. Accordingly, the ray at $\mathbf{r}_{m',p'}^{\text{patch}}$ will have an amplitude of $\tilde{E}_{p',m',n,m,p}^{\text{patch}}$

$$\tilde{E}_{p',m',n,m,p}^{\text{patch}} = \frac{\tilde{E}_{n,m,p}^{\text{obj}}\Gamma\left(\theta_{n,m}^{\text{inc}}\right)\cdot e^{-jk_0\left(\left|\mathbf{r}_{m',p'}^{\text{patch}}-\mathbf{r}_{\text{obj}}\right|\right)}}{1+\left|\mathbf{r}_{m',p'}^{\text{patch}}-\mathbf{r}_{\text{obj}}\right|/\left|\mathbf{r}_{\text{obj}}-\mathbf{r}_{m',p'}^{\text{patch}}\right|} \tag{15}$$

where $\Gamma\left(\theta_{n,m}^{\text{inc}}\right)$ is the total reflection coefficient at the air–object interface S_{obj}.

To characterize the total reflection coefficient $\Gamma\left(\theta_{n,m}^{\text{inc}}\right)$, a 1-D transmission line model along the z-axis is introduced, as shown in Fig. 4. This model can be effective due to the following facts: 1) the electrically large reflectarray is capable of focusing the incident wave into a tiny spot that is much smaller than the object dimensions in the transverse (xy) plane and 2) the dielectric object is located in the far field of each patch element of the reflectarrays such that the plane-wave incidence is a good approximation.

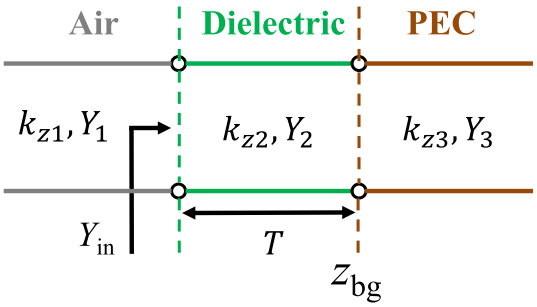

Fig. 4. Transmission line model to characterize the total reflection coefficient $\Gamma\left(\theta_{n,m}^{\text{inc}}\right)$, where k_{zi}, $i \in \{1, 2, 3\}$, is the wavenumber in the z direction for the air, dielectric, and body (PEC) layers, respectively; Y_i is the characteristic admittance for each layer; Y_{in} is the input admittance at the air–object interface; T is the thickness of the dielectric object; and z_{bg} is the background range at the object–body interface S_{bot}.

Denoting k_{zi}, $i \in \{1, 2, 3\}$, as the wavenumber in the z-direction for the air, dielectric, and body (PEC) layer, respectively, the corresponding characteristic admittance Y_i for TE and TM modes can be calculated as follows:

$$Y_i = \begin{cases} \dfrac{\omega\varepsilon_{ri}\varepsilon_0}{k_{zi}}, & \text{for TM mode} \\ \dfrac{k_{zi}}{\omega\mu_0}, & \text{for TE mode} \end{cases} \tag{16}$$

where $k_{zi} = \sqrt{k_0^2\varepsilon_{ri} - k_x^2}$, $k_0^2 = \omega^2\mu\varepsilon_0$, $k_x = k_0 \sin\theta_{m,n}^{\text{inc}}$, ε_0 and μ_0 are the vacuum permittivity and permeability, respectively, and ε_{r1}, ε_{r2}, and ε_{r3} are the relative permittivities of the air, dielectric object, and PEC, respectively. The input admittance Y_{in} at the air–dielectric interface can be written as

$$Y_{\text{in}} = Y_2\frac{Y_3 + jY_2\tan k_{z2}T}{Y_2 + jY_3\tan k_{z2}T}. \tag{17}$$

Accordingly, the total reflection coefficient $\Gamma\left(\theta_{n,m}^{\text{inc}}\right)$ is expressed as

$$\Gamma\left(\theta_{n,m}^{\text{inc}}\right) = \frac{Y_1 - Y_{\text{in}}}{Y_1 + Y_{\text{in}}} \tag{18}$$

where $\Gamma\left(\theta_{n,m}^{\text{inc}}\right)$ has taken an infinite number of reflections inside the dielectric object into consideration.

With the confocal setup of the reflectarrays, the ray is refocused by the p'th reflectarray and directed toward the corresponding p'th feeding antenna located at $\mathbf{r}_{p'}^{\text{feed}}$. The received complex amplitude $\tilde{E}_{n,m,p}^{\text{rec}}$ at $\mathbf{r}_{p'}^{\text{feed}}$ is

$$\tilde{E}_{p',m',n,m,p}^{\text{rec}} = -\tilde{E}_{p',m',n,m,p}^{\text{patch}} \times \frac{e^{-j\left[k_0\left(\left|\mathbf{r}_{p'}^{\text{feed}}-\mathbf{r}_{m',p'}^{\text{patch}}\right|\right)-\Delta\psi_{n,m',p'}\right]}}{1+\left|\mathbf{r}_{p'}^{\text{feed}}-\mathbf{r}_{m',p'}^{\text{patch}}\right|/\left|\mathbf{r}_{m',p'}^{\text{patch}}-\mathbf{r}_{n}^{\text{focus}}\right|} \tag{19}$$

where $\Delta\psi_{n,m',p'}$ is the binary phase compensation added on the m'th patch element of the p'th reflectarray.

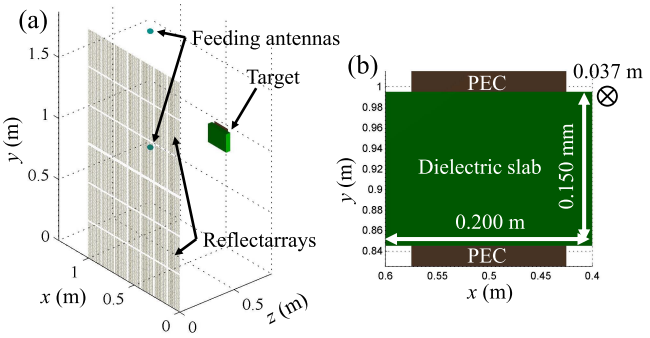

Fig. 5. 3-D setup for simulation and experiment. (a) Two reflectarrays are vertically stacked and fed by two 10-dB standard gain pyramidal horn antennas, operated at 24.16 GHz. (b) Dielectric object is attached to the center of the PEC plate.

Finally, the total received complex amplitude when focusing at $\mathbf{r}_n^{\text{focus}}$ can be calculated by

$$\tilde{E}_n^{\text{rec}} = \sum_{p'=1}^{P}\sum_{m'=1}^{M}\sum_{m=1}^{M}\sum_{p=1}^{P} \tilde{E}_{p',m',n,m,p}^{\text{rec}} \tag{20}$$

where P is the total number of FARAs and M is the total number of patch elements of each reflectarray.

By sweeping ε_r' and ε_r'' of the relative permittivity $\varepsilon_r = \varepsilon_r' - j\varepsilon_r''$ and the thickness T, the analytical received fields $\tilde{E}_n^{\text{rec}}(\varepsilon_r', \varepsilon_r'', T)$, $n \in [1, N]$, N being the total number of focusing points, can be computed. Then, $\tilde{E}_n^{\text{rec}}$ is compared to the measurement E_n^{rec} to find the best matching by minimizing the error function $f(\varepsilon_r', \varepsilon_r'', T)$, namely

$$\{\tilde{\varepsilon}_r', \tilde{\varepsilon}_r'', \tilde{T}\} = \arg\min_{\varepsilon_r', \varepsilon_r'', T} \{f(\varepsilon_r', \varepsilon_r'', T)\}$$
$$\text{s.t. } f(\varepsilon_r', \varepsilon_r'', T) = \sum_{n=1}^{N} \left| \frac{\tilde{E}_n^{\text{rec}}}{\tilde{E}_0^{\text{rec}}} - \frac{E_n^{\text{rec}}}{E_0^{\text{rec}}} \right| \tag{21}$$

where $\tilde{\varepsilon}_r'$, $\tilde{\varepsilon}_r''$, and $\tilde{T}$ are the estimated object dielectric constant, loss factor, and thickness, respectively; and $\tilde{E}_0^{\text{rec}}$ and E_0^{rec} are the calibration amplitudes to normalize the modeled and measured fields, respectively. Note that $\tilde{E}_0^{\text{rec}}$ and E_0^{rec} are independent on the dielectric object under detection and can be obtained in advance by focusing the incident wave at a pure PEC plate located at a range the same as or different from z_{bg}. Theoretically, for the three undetermined parameters, namely T, ε_r', and ε_r'', $N = 3$ measurements will be enough for a successful estimation; however, with a larger value of N, it is possible to achieve a higher estimation accuracy.

IV. Primary Results

To validate the proposed method for object profiles reconstruction and materials identification, both simulation and experiment are carried out. The simulation setup is the same as that in the experiment, which is shown in Fig. 5. Each reflectarray has a side length of 1000 mm. The centers of the top and the bottom reflectarray are located at [500, 1413, 0] and [500, 461, 0] mm, respectively. Two identical 10-dB standard gain pyramidal horn antennas are placed at [1313, 1413, 830] and [1313, 461, 830] mm, respectively. These horn antennas are integrated circulators so that they are operating as transceivers to transmit/receive the single-frequency radar signal to/from the reflectarrays. The radar signal operates at 24.16 GHz, corresponding to a wavelength of $\lambda_0 \approx 12.4$ mm. The dielectric object is a slab that is attached to the center [500, 920, 800] mm of a steel plate ($z_{\text{bg}} = 800$ mm). The slab has the dimensions of 200, 150, and 37 mm in the x-, y-, and z-axes, respectively. Note that the object thickness will be varied in different simulation and experimental cases.

A. Simulation Results

First of all, it is important to examine the imaging resolution of the reflectarray system. Considering the confocal setup of the reflectarray system, the theoretical resolution can be calculated using the well-known Rayleigh criterion [45]

$$\Delta_{\text{lateral}} = \frac{0.4\lambda_0}{\text{NA}}$$
$$\Delta_{\text{axial}} = \frac{1.4\lambda_0}{\text{NA}^2} \tag{22}$$

where the lateral and axial directions correspond to x-/y-axis and z-axis, respectively, and λ_0 is the free-space wavelength at the operating frequency. NA $= (D_0/2R)$ is the so-called numerical aperture (NA), where D_0 is the maximum dimension of the reflectarray aperture and R is the range of the imaging plane. Based on the reflectarray system settings shown in Fig. 5, the estimated imaging resolution is $\sim$4.0 and $\sim$11.2 mm in the lateral and axial directions, respectively.

To further validate the imaging system resolution, the point spread function (PSF) [46] is simulated, which is a common way to show the focusing ability of an antenna array system. Fig. 6(a) and (b) shows the 3-D and 2-D radiation patterns, respectively, when focusing the wave at [500, 920, 800] mm in free space. As anticipated, a sharp focusing spot is achieved. The half 3-dB width of the focusing spot is $\sim\lambda_0/2$ along the x- and y-axes and $\sim\lambda_0$ along the z-axis.

In order to obtain a high calculation efficiency while retaining an acceptable imaging accuracy, the third-order PO is used to calculate the electric and magnetic currents on the dielectric object surface, namely applying (7) with $K = 3$.

First, two lossless dielectric objects are considered in the simulation. Object-1 has a thickness of $T_1 = 20$ mm and a relative permittivity of $\varepsilon_{r1} = 8.0 - j0.0$, whereas Object$-2$ has a thickness of $T_2 = 40$ mm and a relative permittivity of $\varepsilon_{r2} = 2.0 - j0.0$. These two objects, satisfying $T_1\sqrt{\varepsilon_{r1}'} = T_2\sqrt{\varepsilon_{r2}'}$, are selected to verify that the proposed method is able to solve the phase shift ambiguity [47] without loss of generality.

In addition, the general reciprocity theorem described in (9) is applied throughout the simulations to improve the computation efficiency. Its effectiveness is validated in Fig. 7, where the received fields, with and without the reciprocity theorem, are in a good agreement for both Object-1 and Object-2. Fig. 7 also verifies that the near-field radiation pattern of the reflectarray is range-dependent. The magnitude and phase responses of the received fields for the two ambiguous objects differ a lot so that they are distinguished.

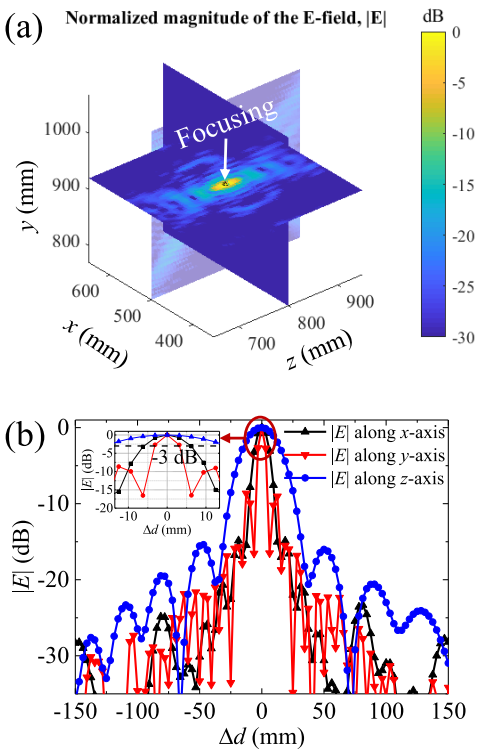

Fig. 6. PSF of the reflectarray imaging system when the focusing is at [500, 920, 800] mm in free space. (a) and (b) 3-D and 2-D radiation patterns, respectively. Δd is the distance between the focusing point and the observation point.

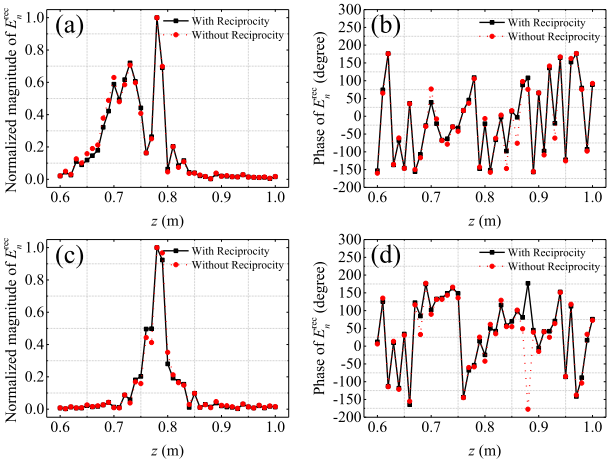

Fig. 7. Received field, with and without applying the reciprocity theorem, for the simulation setup described in Fig. 5. The focusing point is uniformly swept from [500, 920, 600] to [500, 920, 1000] mm along the z-axis. (a) and (b) Calculated magnitude and phase distribution, respectively, for Object−1. (c) and (d) Calculated magnitude and phase distribution, respectively, for Object−2.

Fig. 8(a) and (b) shows the PO simulated target profiles for Object−1 and Object−2, respectively. As it is seen, for Object−1 with an actual thickness of 20 mm, the imaged profile center, thickness, and background range are $[x_{c1}, y_{c1}, z_{c1}] = [500, 920, 780]$ mm, $\tilde{T}_1 = 800 - 780 = 20$ mm, and $z_{bg} = 800$ mm, respectively, which are accurate. However, for Object−2 that has an actual thickness of 40 mm,

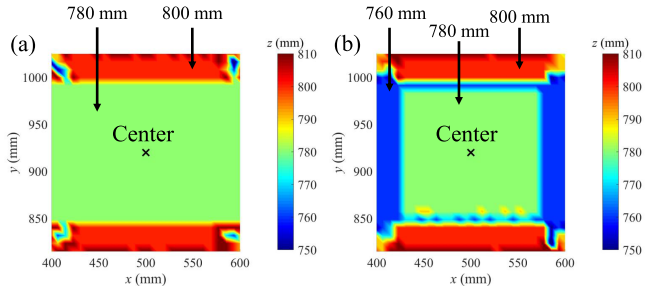

Fig. 8. (a) Simulated target profile for Object−1 ($\varepsilon_{r1} = 8.0 - j0.0$ and $T_1 = 20$ mm). (b) Simulated target profile for Object−2 ($\varepsilon_{r2} = 2.0 - j0.0$ and $T_2 = 40$ mm).

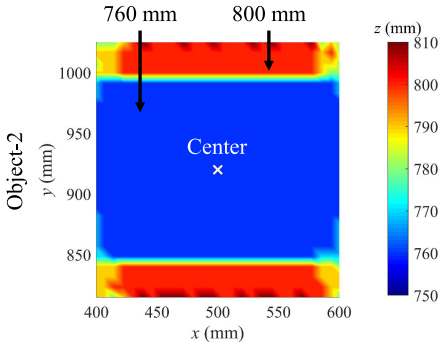

Fig. 9. Simulated target profile for Object−3 ($\varepsilon_{r3} = 4.0 - j0.2$ and $T_3 = 40$ mm).

the imaged profile center and thickness are $[x_{c2}, y_{c2}, z_{c2}] = [500, 920, 780]$ mm and $\tilde{T}_2 = 800 - 780 = 20$ mm, respectively. This error is attributed to the multiple reflections inside the dielectric object so that the focusing position, corresponding to the maximum magnitude of the received field along the z-axis, is achieved underneath the front surface of the dielectric object. When it occurs to a lossy Object−3 with a thickness of $T_3 = 40$ mm and complex relative permittivity of $\varepsilon_{r3} = 4.0 - j0.2$, the magnitude of the multiple reflected waves inside the lossy dielectric slab is considerably degenerated due to the large propagation loss. Thus, the image processing of Object−3 can be similar to that of a metallic object, where the first-order PO method can be sufficient to obtain a quite accurate target profile. The maximum received field along the z-axis can be achieved when the focusing position is at the front surface of the dielectric object. Fig. 9 shows the PO simulated profile of Object−3, where the profile center and thickness are accurately imaged at $[x_{c3}, y_{c3}, z_{c3}] = [500, 920, 760]$ mm and $\tilde{T}_3 = 800 - 760 = 40$ mm, respectively. Considering all aforementioned PO simulation cases, especially for low-loss dielectric, the object permittivity characterization and more accurate object thickness are desired.

Applying the material identification method derived in Section III-B, ε_r' and ε_r'' are swept from 2.0 to 10.0 and from 0 to 0.5, respectively. This sweep range covers most common threat materials, such as narcotics, explosives, and other types of contrabands [48], [49]. The dielectric slab thickness T is swept from 0 to 60 mm. By determining the imaged profile center $[x_c, y_c, z_c]$ for each object, the equally spaced focusing

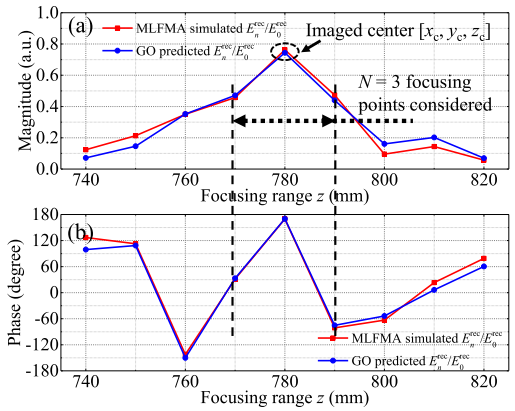

Fig. 10. Best matched (a) magnitude and (b) phase response for Object-1, when the minimum error $\min\{f(\varepsilon_r', \varepsilon_r'', T)\}$ is achieved at $\tilde{\varepsilon}_r' = 8.0$, $\tilde{\varepsilon}_r'' = 0.0$, and $\tilde{T} = 20$ mm.

points can be selected along the range (z-axis)

$$\mathbf{r}_n^{\text{focus}} = \left[x_c, y_c, z_c + \Delta z\left(n - \frac{N+1}{2}\right)\right], \quad n \in [1, N] \qquad (23)$$

where $\Delta z = 10$ mm is the range resolution of the RoI, and total $N = 3$ focusing points are considered for estimating object thickness $\tilde{T}$ and complex relative permittivity $\tilde{\varepsilon}_r = \tilde{\varepsilon}_r' - j\tilde{\varepsilon}_r''$. Those focusing points are selected because they correspond to higher receiving SNR compared to the other focusing points along the $z-$axis and they can potentially eliminate transverse variations of the material property in the transverse (xy) plane, resulting in a higher estimation accuracy at that position.

Fig. 10(a) and (b) shows the best matched magnitude and phase responses for Object-1 when the minimum errors $\min\{f(\varepsilon_r', \varepsilon_r'', T)\}$ are found at $\tilde{\varepsilon}_r' = 8.0$, $\tilde{\varepsilon}_r'' = 0.0$, and $\tilde{T} = 20$ mm. These estimated parameters are the same as the actual ones. Note that more than three focusing points are presented in this figure for the purpose of verifying the accuracy of the GO predicted fields. The error distribution $f(\varepsilon_r', \varepsilon_r'', T)$, obtained when sweeping ε_r', ε_r'', and T, is shown in Fig. 11, where the achieved minimum error is denoted by a solid circle. The same estimation process is performed for Object-2, and the obtained error distribution is shown in Fig. 12. As it is seen, the minimum error $\min\{f(\varepsilon_r', \varepsilon_r'', T)\}$ also happens at the actual object parameters $\tilde{\varepsilon}_r' = 2.0$, $\tilde{\varepsilon}_r'' = 0.0$, and $\tilde{T} = 40$ mm. Therefore, these two ambiguous objects are distinguishable from each other by using the proposed GO estimation method.

Similarly, the error distribution $f(\varepsilon_r', \varepsilon_r'', T)$ for the lossy Object-3 is shown in Fig. 13, where the minimum error is correctly achieved at $\tilde{\varepsilon}_r' = 4.0$, $\tilde{\varepsilon}_r'' = 0.2$, and $\tilde{T} = 40$ mm.

B. Experimental Results

The actual experiment setup to detect a threat object is given in Fig. 14, which indicates all the primary components of the reflectarray system, matching with the simulation setup in Fig. 5. One can refer to the papers see [11], [12]) from the Smiths Detection Inc. for the whole mechanical and electrical design of this commercially available reflectarray imaging system. Here is a brief system description as follows; each of

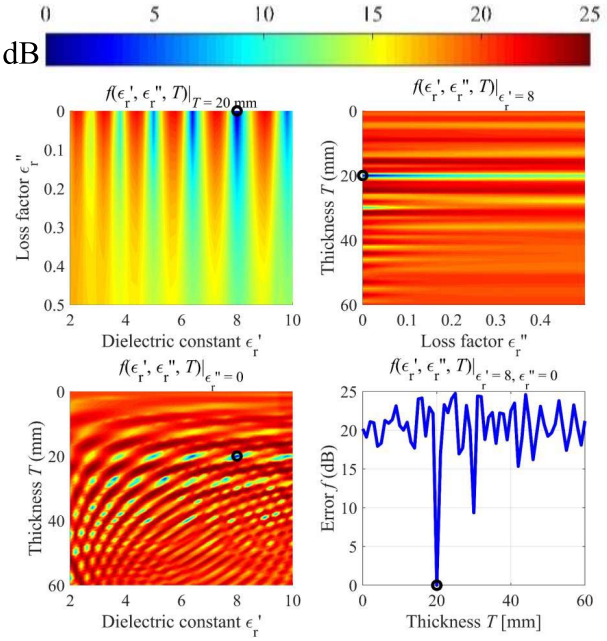

Fig. 11. Error distribution $f(\varepsilon_r', \varepsilon_r'', T)$ for Object-1, obtained by sweeping ε_r', ε_r'', and T, where the minimum error is denoted by a solid circle.

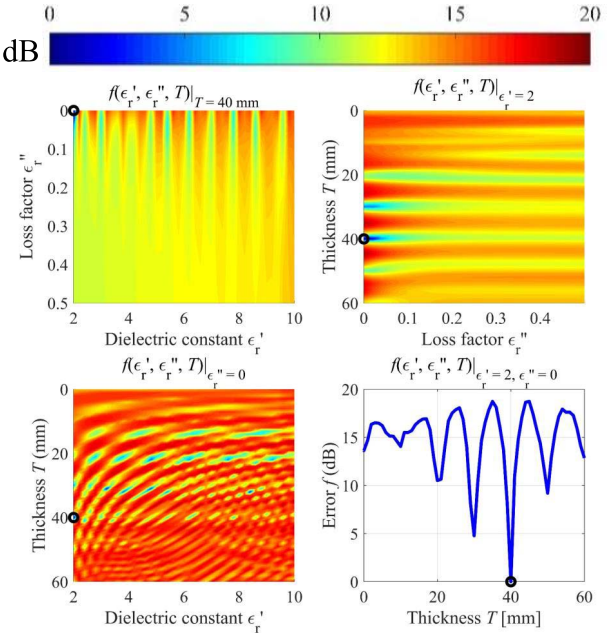

Fig. 12. Error distribution $f(\varepsilon_r', \varepsilon_r'', T)$ for Object-2, obtained by sweeping ε_r', ε_r'', and T, where the minimum error is denoted by a solid circle.

the two reflectorarrays consists of 21 tiles that are fabricated by standard printed circuit board (PCB) techniques. Each tile has total 1008 square microstrip patch antennas that are spaced at $\lambda_0/2$ to minimize the grating lobes. In order to achieve the binary phase shift on each patch antenna, a short-circuited stub loaded with a field-effect transistor (FET) is connected to the feeding line of the patch antenna. The FET operates as an RF switch, making the stub input impedance changed based on the ON/OFF state of the FET, which eventually gives rise to the phase change of the reflection coefficients (the magnitude will remain nearly the same). The dimensions of the stub and the

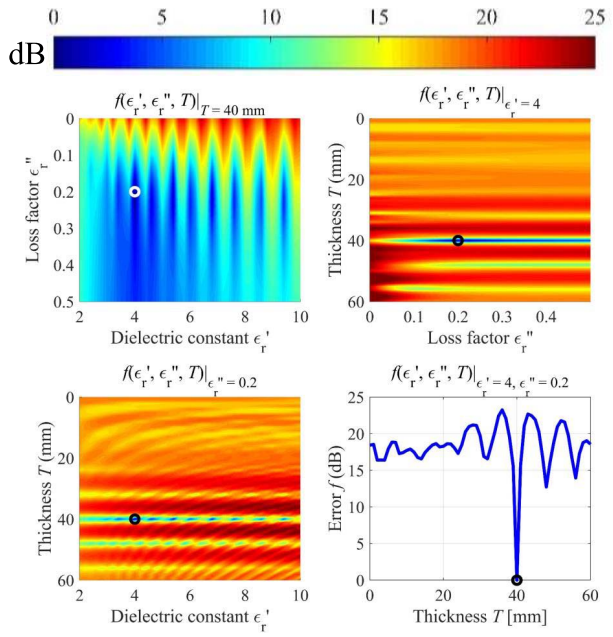

Fig. 13. Error distribution $f(\varepsilon_r', \varepsilon_r'', T)$ for Object-3, obtained by sweeping ε_r', ε_r'', and T, where the minimum error is denoted by a solid circle.

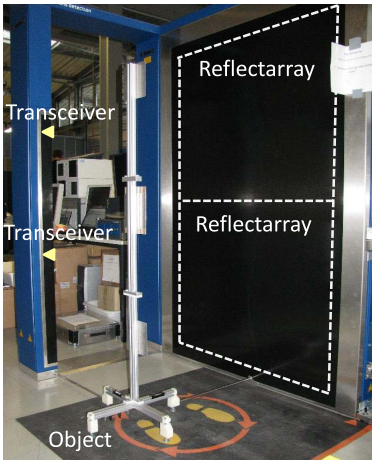

Fig. 14. Experimental setup of the reflectarray screening system from Smiths Detection Inc.

patch antenna have to be optimized with full-wave simulations so that the reflection phase changes by 180° when the FET switches.

Note that the theoretical imaging resolution [see (22)] and the simulated PSF (Fig. 6) of the reflectarray system have been presented in Section IV-A. To further evaluate the imaging resolution experimentally, the measurement of the PSF can be performed. However, this is avoided in this article since the previous experiment (see [12, Fig. 8]) using the same reflectarray system has shown that the smallest objects that are visible are 4 mm × 4 mm metal shims. It is generally accepted that a people-screening system with near or less than 1-cm resolution is working properly and will be sufficient for detecting common threat objects, such as metallic weapons or explosive items [48], [49].

The calibration measurement has to be performed first before the object imaging. There are mainly two different

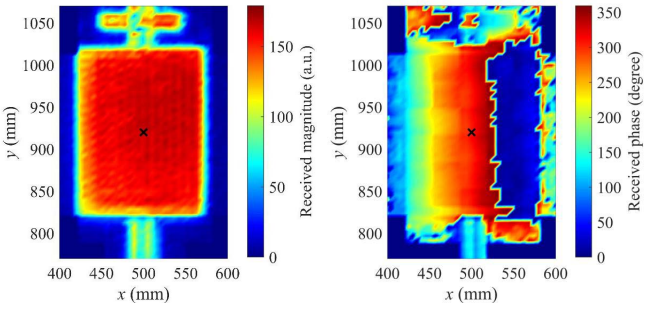

Fig. 15. Calibration measurement for the amplitude regularization, which includes the magnitude distribution (left) and the phase distribution (right).

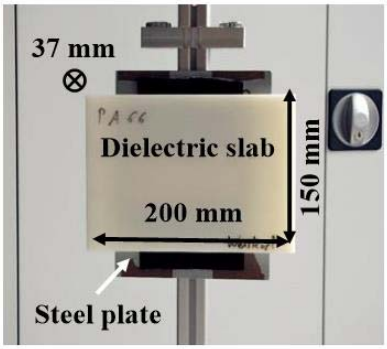

Fig. 16. Polyamide-6, 6 (PA66) object under detection. The size of the dielectric is 200 mm × 150 mm × 37 mm, which is attached to the center of the steel plate.

steps. The first calibration step is the background measurement, where an empty imaging domain with no object inside is scanned and the corresponding measured signal amplitude is saved as E_n^{bg}, n being the index of the focusing point. Accordingly, E_n^{bg} will be subtracted from all the new measurements E_n^{meas} with objects placed in the imaging domain to obtain a background-removed measurement of E_n^{rec}, namely

$$E_n^{\text{rec}} = E_n^{\text{meas}} - E_n^{\text{bg}}. \tag{24}$$

The second calibration step is to measure the calibration amplitude E_0^{rec} to regularize (or normalize) the measured fields E_n^{rec}, which also has to be background-removed. In this article, this measurement is done by focusing the incident wave at the center of the pure steel plate, which is at $[x, y, z] = [520, 920, 800]$ mm. The typical measured amplitude (including the magnitude and phase distributions) of a pure steel plate is given in Fig. 15. The center cross denotes the position where the calibration amplitude E_0^{rec} is selected. Note that the experimental settings have to be matched with those in the forward model so that E_n^{rec} and E_0^{rec} can be used in (21) for a successful object material characterization.

To evaluate the material characterization algorithm, a dielectric brick is selected, named Object-4. As shown in Fig. 16, the object is a dielectric slab made of polyamide-6, 6 (PA66), which has a relative dielectric constant of $2.8 \sim 3.1$ and a low-loss tangent of $\tan\sigma < 0.01$ at K-band [50]. The size of the dielectric is 200 mm × 150 mm × 37 mm.

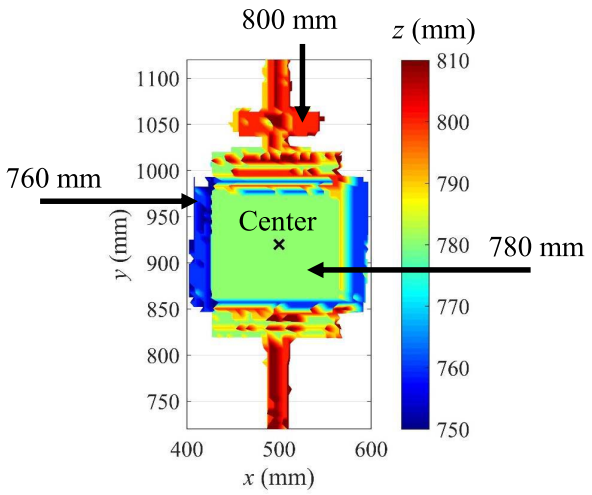

Fig. 17. Experimentally reconstructed target profile, where the imaged thickness and profile center are 20 and [500, 920, 780] mm, respectively.

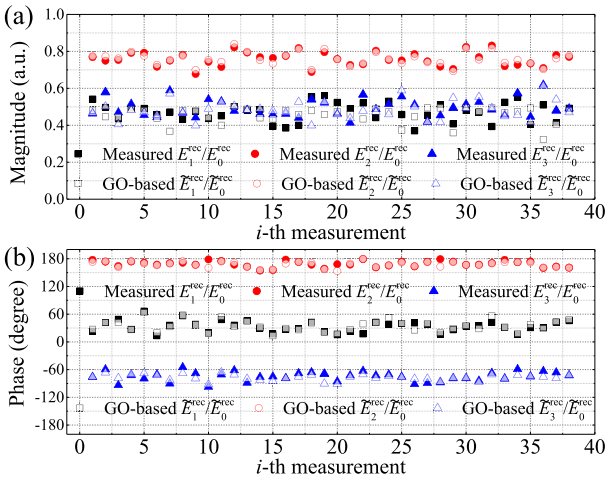

Fig. 18. Best matched (a) magnitude and (b) phase responses between the measured electric fields E_n^{rec} and GO predicted $\tilde{E}_n^{\text{rec}}$, where the three considered focusing points are defined in (23) with $N = 3$.

The dielectric slab is attached to the center of a steel plate by a 1.0 mm ($< \lambda_0/10$) Velcro layer. To predict the received amplitude $\tilde{E}_n^{\text{rec}}(\varepsilon_r', \varepsilon_r'', T)$ using the GO forward model described in Fig. 3, the Velcro layer is approximated to be a layer of air. Therefore, the transmission line model in Fig. 4 to calculate the total reflection coefficient $\Gamma\left(\theta_{n,m}^{\text{inc}}\right)$ is modified to include four cascaded layers, namely air–dielectric–air PEC.

Fig. 17 shows the experimentally reconstructed target profile. The imaged profile center is at [500, 920, 780] mm, which has an imaged thickness of $800 - 780 = 20$ mm that is much smaller than the actual object thickness of 37 mm. This happens due to the strong multiple reflections within the dielectric slab makes the maximum magnitude of the received field along the z-axis achieved under the front surface of the dielectric object. A similar explanation has been demonstrated for the simulation results in Fig. 8(b).

To estimate the complex relative permittivity $\tilde{\varepsilon}_r = \tilde{\varepsilon}_r' - j\tilde{\varepsilon}_r''$ and a more precise thickness $\tilde{T}$, ε_r', ε_r'', and T are swept to

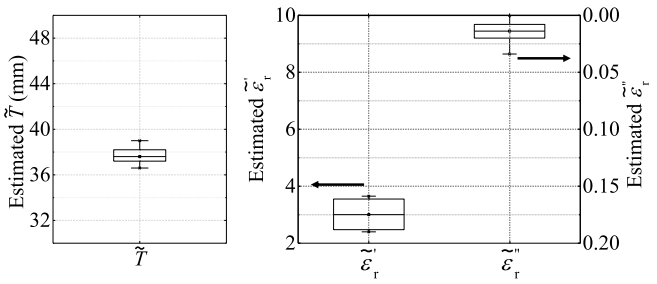

Fig. 19. Experimentally estimated dielectric constant $\tilde{\varepsilon}_r'$, loss factor $\tilde{\varepsilon}_r''$, and thickness $\tilde{T}$ of the PA66 dielectric slab.

TABLE I

ESTIMATED RESULTS ON THE THICKNESS $\tilde{T}$ AND COMPLEX RELATIVE PERMITTIVITY $\tilde{\varepsilon}_r = \tilde{\varepsilon}_r' - j\tilde{\varepsilon}_r''$ FOR THE PA66 SLAB

Values	$\tilde{T}$	$\tilde{\varepsilon}_r'$	$\tilde{\varepsilon}_r''$
Mean	37.6 mm	3.012	0.014
Standard deviation	0.593 mm	0.425	0.009

compute the GO predicted received amplitudes $\tilde{E}_n^{\text{rec}}(\varepsilon_r', \varepsilon_r'', T)$. The sweeping ranges of ε_r', ε_r'', and T are the same as those specified in the simulations. Then, $\tilde{E}_n^{\text{rec}}$ is compared to the experimental measurement E_n^{rec} to find the best matched magnitude and phase responses using (21). The estimation is repeated 38 times, and Fig. 18(a) and (b) shows the best matched magnitude and phase responses between the measured fields E_n^{rec} and GO predicted fields $\tilde{E}_n^{\text{rec}}(\tilde{\varepsilon}_r', \tilde{\varepsilon}_r'', \tilde{T})$ during each estimation process, respectively. As we can see, both $\tilde{E}_2^{\text{rec}}$ and E_2^{rec} are well-matched and achieve their maximum magnitude at the range $z = 780$ mm, which is accordance with the experimentally reconstructed target profile in Fig. 17.

The entire estimated results for $\tilde{\varepsilon}_r'$, $\tilde{\varepsilon}_r''$, and $\tilde{T}$ of the PA66 slab are given in Fig. 19. Table I shows the mean values for $\tilde{\varepsilon}_r'$, $\tilde{\varepsilon}_r''$, and $\tilde{T}$ are 3.012, 0.014, and 37.6 mm, respectively; and the standard deviations for $\tilde{\varepsilon}_r'$, $\tilde{\varepsilon}_r''$, and $\tilde{T}$ are 0.425, 0.009, and 0.593 mm, respectively. The estimation error can be attributed to the noisy experimental measurement as well as the minor approximation error from the four-layer transmission line model.

V. CONCLUSION

This article first presents a PO-based simulation method to facilitate the design of a multireflectarray system. Then, an object material characterization method using GO is derived for such a system. The characterization process not only retrieves the complex relative permittivity of the object but also improves the profile reconstruction performance in terms of a more accurate object thickness. Both simulations and experiments have been carried out to verify the effectiveness and efficiency of the proposed methods.

Note that the object profile imaging by the reflectarray system has a fast speed of ~14 frames/s. This is due to the simple range projection algorithm as given in (11). Then,

the material characterization algorithm is performed on a desktop based on the Intel i7-4790 Processor with total of four cores and eight threads, which results in an reconstruction speed of ∼4 frames/s. Thus, the overall image formation speed of the reflectarray system is ∼3 frames/s. Further speed improvement can be achieved based on more CPU threads; thus, the imaging system can be operated in real time to display the imaged object information, including the 3-D range profile and the complex permittivity.

When accessible to a well-defined database with the knowledge of the permittivities of typical threat materials, the proposed detection methodology is capable of accurately suggesting threat identities based on the detected object profiles and permittivities, which can have a variety of applications in security screening checkpoints at train stations, airports, and many other public and private facilities to predict potential threats.

ACKNOWLEDGMENT

The authors would like to thank Smiths Detection Inc. for collecting the data with their Eqo system.

REFERENCES

[1] D. M. Sheen, D. L. Mcmakin, and T. E. Hall, "Three-dimensional millimeter-wave imaging for concealed weapon detection," *IEEE Trans. Microw. Theory Techn.*, vol. 49, no. 9, pp. 1581–1592, Sep. 2001.

[2] S. Ahmed, A. Schiessl, F. Gumbmann, M. Tiebout, S. Methfessel, and L.-P. Schmidt, "Advanced microwave imaging," *IEEE Microw. Mag.*, vol. 13, no. 6, pp. 26–43, Sep. 2012.

[3] T. Liu, Y. Zhao, Y. Wei, Y. Zhao, and S. Wei, "Concealed object detection for activate millimeter wave image," *IEEE Trans. Ind. Electron.*, vol. 66, no. 12, pp. 9909–9917, Dec. 2019.

[4] E. C. Fear, J. Bourqui, C. Curtis, D. Mew, B. Docktor, and C. Romano, "Microwave breast imaging with a monostatic radar-based system: A study of application to patients," *IEEE Trans. Microw. Theory Techn.*, vol. 61, no. 5, pp. 2119–2128, May 2013.

[5] I. Walterscheid, J. H. G. Ender, A. R. Brenner, and O. Loffeld, "Bistatic SAR processing and experiments," *IEEE Trans. Geosci. Remote Sens.*, vol. 44, no. 10, pp. 2710–2717, Oct. 2006.

[6] L. E. Tirado, W. Zhang, A. Bisulco, H. Gomez-Sousa, and J. A. Martinez-Lorenzo, "Towards three-dimensional millimeter-wave radar imaging of on-the-move targets," in *Proc. IEEE Int. Symp. Antennas Propag. USNC/URSI Nat. Radio Sci. Meeting*, Jul. 2018, pp. 1959–1960.

[7] D. L. Donoho, "Compressed sensing," *IEEE Trans. Inf. Theory*, vol. 52, no. 4, pp. 1289–1306, Apr. 2006.

[8] Y. Rodriguez-Vaqueiro, Y. Alvarez Lopez, B. Gonzalez-Valdes, J. A. Martinez, F. Las-Heras, and C. M. Rappaport, "On the use of compressed sensing techniques for improving multistatic millimeter-wave portal-based personnel screening," *IEEE Trans. Antennas Propag.*, vol. 62, no. 1, pp. 494–499, Jan. 2014.

[9] W. Zhang *et al.*, "Experimental results of a 3-D millimeter-wave compressive reflector antenna imaging system," *IEEE Antennas Wireless Propag. Lett.*, vol. 18, no. 1, pp. 24–28, Jan. 2019.

[10] M. Soumekh, *Synthetic Aperture Radar Signal Processing*. Hoboken, NJ, USA: Wiley, 1999.

[11] P. Corredoura, Z. Baharav, B. Taber, and G. Lee, "Millimeter-wave imaging system for personnel screening: Scanning 10^7 points a second and using no moving parts," *Proc. SPIE*, vol. 6211, May 2006, Art. no. 62110B.

[12] B. N. Lyons, E. Entchev, and M. K. Crowley, "Reflect-array based mm-Wave people screening system," *Proc. SPIE*, vol. 8900, Oct. 2013, Art. no. 890002.

[13] H. Gomez-Sousa and J. A. Martinez-Lorenzo, "Modeling and imaging security threats using a single-frequency adaptable reflect-array," in *Proc. IEEE Int. Symp. Technol. Homeland Secur. (HST)*, Apr. 2017, pp. 1–7.

[14] J. Huang, "Microstrip reflectarray," in *Proc. Antennas Propag. Soc. Symp. Dig.*, 1991, pp. 612–615.

[15] D. M. Pozar, S. D. Targonski, and H. D. Syrigos, "Design of millimeter wave microstrip reflectarrays," *IEEE Trans. Antennas Propag.*, vol. 45, no. 2, pp. 287–296, Feb. 1997.

[16] J. Song, C.-C. Lu, and W. Cho Chew, "Multilevel fast multipole algorithm for electromagnetic scattering by large complex objects," *IEEE Trans. Antennas Propag.*, vol. 45, no. 10, pp. 1488–1493, 1997.

[17] W. C. Gibson, *The Method of Moments in Electromagnetics*. Boca Raton, FL, USA: CRC Press, 2014.

[18] W. Baukus, "X ray imaging for on-the-body contraband detection," in *Proc. 16th Annu. Secur. Technol. Symp. Exhib.*, 2000.

[19] S. Ahmed *et al.*, "Qpass quick personnel automatic safe screening for security enhancement of passengers," in *Proc. Future Secur. Conf.*, 2011.

[20] O. Yurduseven, "Indirect microwave holographic imaging of concealed ordnance for airport security imaging systems," *Prog. Electromagn. Res.*, vol. 146, pp. 7–13, 2014.

[21] J. C. Weatherall, J. Barber, and B. T. Smith, "Spectral signatures for identifying explosives with wideband millimeter-wave illumination," *IEEE Trans. Microw. Theory Techn.*, vol. 64, no. 3, pp. 999–1005, Mar. 2016.

[22] M. E. Baginski, D. L. Faircloth, and M. D. Deshpande, "Comparison of two optimization techniques for the estimation of complex permittivities of multilayered structures using waveguide measurements," *IEEE Trans. Microw. Theory Techn.*, vol. 53, no. 10, pp. 3251–3259, Oct. 2005.

[23] A. Zamani and A. M. Abbosh, "Estimation of frequency dispersive complex permittivity seen by each antenna for enhanced multistatic radar medical imaging," *IEEE Trans. Antennas Propag.*, vol. 65, no. 7, pp. 3702–3711, Jul. 2017.

[24] C. P. Gallagher, N. Cole, P. P. Savage, C. Mckeever, J. R. Sambles, and A. P. Hibbins, "A broadband stripline technique for characterizing relative permittivity and permeability," *IEEE Trans. Microw. Theory Techn.*, vol. 67, no. 1, pp. 231–238, Jan. 2019.

[25] D. W. Winters, E. J. Bond, B. D. Van Veen, and S. C. Hagness, "Estimation of the frequency-dependent average dielectric properties of breast tissue using a time-domain inverse scattering technique," *IEEE Trans. Antennas Propag.*, vol. 54, no. 11, pp. 3517–3528, Nov. 2006.

[26] K. K. M. Chan, A. E.-C. Tan, L. Li, and K. Rambabu, "Material characterization of arbitrarily shaped dielectrics based on reflected pulse characteristics," *IEEE Trans. Microw. Theory Techn.*, vol. 63, no. 5, pp. 1700–1709, May 2015.

[27] J. Bourqui and E. C. Fear, "System for bulk dielectric permittivity estimation of breast tissues at microwave frequencies," *IEEE Trans. Microw. Theory Techn.*, vol. 64, no. 9, pp. 3001–3009, Sep. 2016.

[28] W. B. Weir, "Automatic measurement of complex dielectric constant and permeability at microwave frequencies," *Proc. IEEE*, vol. 62, no. 1, pp. 33–36, Jan. 1974.

[29] M. B. Abdillah, B. Lyons, and E. Entchev, "Identification of potential threat materials using active electromagnetic waves," *Mar. 5*, vol. 2013, uS Patent 8,390,504.

[30] M. A. Islam, A. Kiourti, and J. L. Volakis, "A novel method of deep tissue biomedical imaging using a wearable sensor," *IEEE Sensors J.*, vol. 16, no. 1, pp. 265–270, Jan. 2016.

[31] J. Barowski, M. Zimmermanns, and I. Rolfes, "Millimeter-wave characterization of dielectric materials using calibrated FMCW transceivers," *IEEE Trans. Microw. Theory Techn.*, vol. 66, no. 8, pp. 3683–3689, Aug. 2018.

[32] J. Roelvink and S. Trabelsi, "Measuring the complex permittivity of thin grain samples by the free-space transmission technique," in *Proc. IEEE Int. Instrum. Meas. Technol. Conf.*, May 2012, pp. 310–313.

[33] K. Y. You, M. S. Sim, H. Mutadza, F. Esa, and Y. L. Chan, "Free-space measurement using explicit, reference-plane and thickness-invariant method for permittivity determination of planar materials," in *Proc. Prog. Electromagn. Res. Symp. Fall (PIERS-FALL)*, Nov. 2017, pp. 222–228.

[34] S. V. Hum, M. Okoniewski, and R. J. Davies, "Realizing an electronically tunable reflectarray using varactor diode-tuned elements," *IEEE Microw. Wireless Compon. Lett.*, vol. 15, no. 6, pp. 422–424, Jun. 2005.

[35] E. Carrasco, M. Barba, and J. A. Encinar, "X-band reflectarray antenna with switching-beam using PIN diodes and gathered elements," *IEEE Trans. Antennas Propag.*, vol. 60, no. 12, pp. 5700–5708, Dec. 2012.

[36] H. Theissen, C. Dahl, I. Rolfes, and T. Musch, "An electronically reconfigurable reflectarray element based on binary phase shifters for K-band applications," in *Proc. German Microw. Conf. (GeMiC)*, Mar. 2016, pp. 321–324.

[37] S. Park, S. Kim, D. K. Kim, J. Choi, and K.-Y. Jung, "Numerical study on the feasibility of a 24 GHz ISM-band Doppler radar antenna for near-field sensing of human respiration in electromagnetic aspects," *Appl. Sci.*, vol. 10, no. 18, p. 6159, Sep. 2020.
[38] C. Will, P. Vaishnav, A. Chakraborty, and A. Santra, "Human target detection, tracking, and classification using 24-GHz FMCW radar," *IEEE Sensors J.*, vol. 19, no. 17, pp. 7283–7299, Sep. 2019.
[39] S. Gabriel, R. W. Lau, and C. Gabriel, "The dielectric properties of biological tissues: II. Measurements in the frequency range 10 hz to 20 GHz," *Phys. Med. Biol.*, vol. 41, no. 11, pp. 2251–2269, Nov. 1996.
[40] C. A. Balanis, *Advanced Engineering Electromagnetics*, 2nd ed. Hoboken, NJ, USA: Wiley, 2012.
[41] J. G. Meana, J. Á. Martinez-Lorenzo, F. Las-Heras, and C. Rappaport, "Wave scattering by dielectric and lossy materials using the modified equivalent current approximation (MECA)," *IEEE Trans. Antennas Propag.*, vol. 58, no. 11, pp. 3757–3761, Nov. 2010.
[42] J. Gutiérrez-Meana, J. A. Martínez-Lorenzo, and F. Las-Heras, "High frequency techniques: The physical optics approximation and the modified equivalent current approximation (MECA)," in *Electromagnetic Waves Propagation in Complex Matter*. Rijeka, Croatia: InTech, 2011.
[43] W. Zhang and J. A. Martinez-Lorenzo, "Single-frequency material characterization using a microwave adaptive reflect-array," in *Proc. IEEE Int. Symp. Antennas Propag. USNC/URSI Nat. Radio Sci. Meeting*, Jul. 2018, pp. 1063–1064.
[44] M. H. Umari, D. K. Ghodgaonkar, V. V. Varadan, and V. K. Varadan, "A free-space bistatic calibration technique for the measurement of parallel and perpendicular reflection coefficients of planar samples," *IEEE Trans. Instrum. Meas.*, vol. 40, no. 1, pp. 19–24, 1991.
[45] K. R. Spring, T. J. Fellers, and M. W. Davidson, "Resolution and contrast in confocal microscopy," Nat. High Magn. Field Lab., Florida State Univ., Tallahassee, FL, USA, Tech. Rep., 2006. [Online]. Available: https://www.olympus-lifescience.com/en/microscope-resource/primer/techniques/confocal/resolutionintro/
[46] P. J. Shaw and D. J. Rawlins, "The point-spread function of a confocal microscope: Its measurement and use in deconvolution of 3-D data," *J. Microsc.*, vol. 163, no. 2, pp. 151–165, Aug. 1991, doi: 10.1111/j.1365-2818.1991.tb03168.x.
[47] S. Trabelsi, A. W. Kraszewski, and S. O. Nelson, "Phase-shift ambiguity in microwave dielectric properties measurements," *IEEE Trans. Instrum. Meas.*, vol. 49, no. 1, pp. 56–60, Feb. 2000.
[48] D. G. Watters, D. G. Falconer, K. J. Harker, R. Ueberschaer, and A. J. Bahr, "Microwave inspection of luggage for contraband materials using imaging and inverse-scattering algorithms," *Res. Nondestruct. Eval.*, vol. 7, no. 1, pp. 153–168, 1995.
[49] E. M. A. Hussein and E. J. Waller, "Review of one-side approaches to radiographic imaging for detection of explosives and narcotics," *Radiat. Meas.*, vol. 29, no. 6, pp. 581–591, Dec. 1998.
[50] A. R. Von Hippel, *Dielectric Materials and Applications*. New York, NY, USA: Wiley, 1954.

Weite Zhang received the B.Sc. degree in electrical engineering from the Zhejiang University of Technology, Hangzhou, China, in 2014, and the M.Sc. degree in electrical engineering from Zhejiang University, Hangzhou, China, in 2017. He is currently pursuing the Ph.D. degree in electrical engineering at Northeastern University, Boston, MA, USA.

His research interest includes wireless communication and millimeter-wave imaging systems.

Hipolito Gomez-Sousa (Senior Member, IEEE) was a Post-Doctoral Fellow with Northeastern University, Boston, MA, USA, from February 2016 to January 2017. He has been a Post-Doctoral Fellow with the University of Vigo, Vigo, Spain, since 2019. His research interest includes computational electromagnetic modeling for microwave and millimeter-wave imaging applications.

Juan Heredia-Juesas received the Ph.D. degree in telecommunications engineering from the University of Oviedo, Oviedo, Spain, in 2014.

He is currently a Post-Doctoral Research Associate with Northeastern University, Boston, MA, USA. His current research interests include signal theory, signal processing, spectral analysis, machine learning, deep learning, and imaging, optimization, and distributed algorithms.

Jose A. Martinez-Lorenzo (Senior Member, IEEE) received the B.S. and M.S./Ph.D. degrees from the University of Vigo, Vigo, Spain, in 2002 and 2005, respectively.

He is currently an Associate Professor with the Department of Mechanical and Industrial Engineering and the Department of Electrical and Computer Engineering, Northeastern University, Boston, MA, USA. He is also the Director of the Sensing Imaging Control and Actuation Laboratory, Northeastern University. He has authored over 200 technical journal and conference papers. His research interests include high-capacity sensing and imaging systems.

Dr. Martinez-Lorenzo was a recipient of the 2017 NSF Early CAREER Award. He also serves as an Associate Editor for the IEEE TRANSACTIONS ON ANTENNAS AND PROPAGATION.